Characterization of transversely confined electron beam-generated plasma using two-dimensional particle-in-cell simulations

Qinchuang Cao[1, †], Jian Chen[1, †], Haomin Sun[2], Guangyu Sun[2], Shigui Liu[3,4], Chang Tan[3,4], Zhibin Wang[1,*]

[1]Sino-French Institute of Nuclear Engineering and Technology, Sun Yat-sen University, Zhuhai 519082, China

[2]École Polytechnique Fédérale de Lausanne (EPFL), Swiss Plasma Center (SPC), CH-1015 Lausanne, Switzerland

[3]Shaanxi Key Laboratory of Plasma Physics and Applied Technology, Xi'an 710100, China

[4]Xi'an Aerospace Propulsion Institute, Xi'an 710100, China

[*]Corresponding Author: wangzhb8@sysu.edu.cn

[†]These two authors contribute equally to this work

Abstract

Electron beam-generated plasmas (EBPs) have been used to modify the surface properties. In certain applications, EBPs are transversely confined and their properties are of value to the treatment. In this paper, the characteristics of an electron beam-generated argon plasma, confined within a narrow gap, are investigated using a two-dimensional particle-in-cell simulation. The employed particle-in-cell/Monte Carlo collision model accounts for the electron and ion kinetics, as well as collisions between electrons and the background gas including the elastic scattering, excitation and impact ionization. Our simulations reveal a strong correlation between the plasma density and the beam density within the plasma bulk. The excitation of obliquely growing waves is observed, which is found to have a significant impact on the transport of beam electrons, thereby leading to the non-uniformities of plasma density and electron temperature. Specifically, the obliquely growing waves increase the local plasma density while reducing the electron temperature. These contrasting effects compensate

for each other, and therefore, to some extent, smooth out the distributions of ion flux and energy flux. We further examine the variations of plasma parameters with respect to the beam current density, beam energy, and gas pressure. Increasing the beam current density or decreasing the beam energy result in higher plasma density and electron temperature, while increasing pressure leads to a higher plasma density but electron temperature scarcely changes. Based on the simulation results, we propose an approach to achieve independent control of the ion flux and energy flux by adjusting beam current density, beam energy, and pressure.

Keywords: Electron beam-generated plasma, plasma discharge, particle-in-cell simulation

I. Introduction

Electron beam-generated plasmas (EBPs) exhibit wide parameter windows in plasma density and temperature, making them suitable for various applications such as material processing [1-3], coating [4, 5] and outer space investigations [6, 7]. In certain applications, such as treating inner surfaces of tubular apparatuses or vessel-like cavities, EBPs are transversely confined within narrow gaps comparable to the electron beam radius [8]. Under these conditions, the characteristic length of the system may become smaller than the beam energy relaxation scale, resulting in changes in beam transport comparing to traditional electron beam-plasma interaction scenario [9]. Consequently, plasma properties in bounded EBPs may deviate from those in unbounded EBPs due to different beam behaviors [10-12].

Significant efforts have been dedicated to experimental investigations of EBP properties in narrow gaps [13-15]. For instance, Burdovitsin et al. developed an EBP platform to enhance the applicability of EBP in ion-plasma surface modification [13,14]. Electron beam is generated by a forevacuum plasma-cathode electron source and transferred into a biased long metal tube, producing the EBPs there. Experimental results showed that the current flow to the walls exhibit a non-monotonic distribution with a minimum in the middle, indicating the large non-uniformities of generated EBPs. In contrast to experimental investigations, numerical simulations offer a wealth of diagnostic data, enabling a meticulous examination of the underlying physics. So far, a large number of numerical studies have been performed to enhance the understanding of the discharge characteristics of EBPs, primarily by means of fluid and kinetic approaches [16-21]. Rauf et al. developed a three-dimensional hybrid model to investigate the magnetized EBPs. The results showed that the non-uniformities in plasmas arise from the asymmetry of the chamber combined with the $E \times B$ drift [19]. Furthermore, they recently performed 2D particle-in-cell/Monte Carlo collision (PIC/MCC) simulations to investigate the influence of magnetic fields on electron transport in EBPs [20]. Chelvam et al. [17] formulated a 2D fluid model that accounts for plasma-wall interactions and particle reactions. Their simulation results demonstrated the tunability of discharge current, voltage, and power dissipation by manipulating electron beam parameters. Wang et al. [21] employed a 1D PIC/MCC model to simulate electron beam driven micro-discharge. Their computational

study presented comprehensive plasma properties under different operational conditions, and the strategies for achieving low energy and high ion flux were discussed based on simulation results.

Despite the success of previous studies in unraveling the properties of EBPs, a gap persists in this research field. The majority of these studies either do not utilize fully kinetic approaches for multi-dimensional simulations or solely rely on the simplifying assumptions of one-dimensional (1D) kinetic approaches. The kinetic effects on EBP characteristics, such as the interaction between waves and particles, are not fully appreciated in a multi-dimensional sense. This limitation highlights the need for a multi-dimensional kinetic simulation to comprehensively explore the characteristics of EBPs. On the other hand, the understanding of EBPs transversely confined in a long narrow gap is still limited, as a comprehensive numerical study for this setup is absent, to the best of our knowledge. Therefore, there is a strong motivation to conduct a comprehensive multiple-dimensional kinetic simulation to characterize the plasma properties of transversely confined EBPs in real devices.

In this paper, we present a numerical study using a 2D3V particle-in-cell/Monte Carlo collision (PIC/MCC) model to simulate full-size EBP discharges within a long narrow gap. It is, to our knowledge, the first reported study of this kind. The employed PIC/MCC model incorporates the electron and ion kinetics as well as the electron-neutral collisions including the elastic scattering, excitation and impact ionization. The primary focus of this paper is to characterize the properties of EBPs and explore the influence of various operating conditions on the plasma behavior. Moreover, the effects of plasma waves on the plasma parameters are examined and discussed. The paper also explores the variations in plasma properties resulting from changes in beam current densities, beam electron energies, and gas pressures. Effective means to tune the ion flux and ion energy flux for EBPs transversely confined in a long narrow gap are also discussed, which offers practical strategies for optimizing the performance of such systems.

This paper is organized as follows: In Section II, the employed PIC/MCC model is described. Simulation results are presented and discussed in Section III, and a summary is provided in Section IV.

4

II. Numerical Model

In this study, a two-dimensional calculation domain is adopted to simulate the EBP discharges in a long narrow gap, as depicted in Fig. 1. The chosen domain closely resembles the configuration of the EBP platform's long metal tube in Ref. [14]. To simplify the computational model, a slab geometry is employed in this paper instead of the actual cylindrical shape of the system. Furthermore, to optimize computational efficiency, we take advantage of the symmetry along the y-axis (or $x=0$) by simulating only half of the configuration. A reflected boundary condition is imposed at the top boundary ($x=0$), allowing particles passing through this boundary to be reflected at the same position with reversed perpendicular velocity. The transverse and longitudinal lengths of the simulation domain are denoted as $L_x=5$ mm and $L_y=200$ mm, respectively. A grounded injection electrode is located at the left boundary with the length 3.3 mm. An intense mono-energetic beam is launched along y direction from this injection electrode. The beam current density, J_b, and beam energy, ε_b, are varied within the ranges of 300-1000 A/m² and 2-8 keV, respectively. Two metal electrodes are placed at the bottom and right boundaries ($x=L_x$ and $y=L_y$, respectively). These electrodes are grounded. A Neumann boundary condition of electric field is implemented at the left boundary between the injection electrode and the metal wall electrode. Particles that hit these two metal electrodes and left boundary are assumed to be fully absorbed. The secondary electron emission is disabled presently in this paper. This approach is justified by the low sheath voltage drop for the cases of interest in this work. Similar practices have been adopted in various previous numerical studies [20-22]. The domain is filled with argon as the background gas and the gas pressure p is varied within the range of 3~9 Pa. Only the electrons and singly-charged Ar^+ are considered in the simulations.
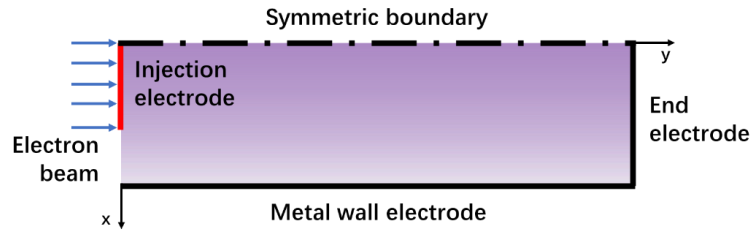

Fig. 1 Schematic diagram of the simulation domain

All the simulations in this study are performed using the open-source EDIPIC-2D code. EDIPIC-2D is a parallelized explicit electrostatic PIC code resolving two coordinates and three velocity components (2D3V). In EDIPIC-2D code, particles are advanced using the Boris scheme, and the electric field is obtained by solving the Poisson's equation in Cartesian geometry [23, 24]. Besides the kinetic PIC model, EDIPIC-2D also includes a Monte-Carlo Collision (MCC) model for the electron-neutral and ion-neutral collisions. EDIPIC-2D is also equipped with a range of diagnostics to facilitate in-depth analysis of the simulation results. For more comprehensive information about the capabilities and methodologies employed in EDIPIC-2D, we refer readers to Ref. [25, 26]. EDIPIC-2D has undergone benchmarking against multiple codes [27-29] and successfully applied to EBP simulations as recently reported in Rauf et al.'s paper [20].

Since we only care about the plasma properties at steady state, it is reasonable that the simulations start from an initial plasma to reduce the computational time for density buildup process. The initial plasma parameters are set as follows: the initial uniform plasma density $n_{p0}=n_{e0}=n_{i0}=10^{16}$ m^{-3}, the initial electron temperature $T_{e,0}=4.0$ eV and the initial ion temperature is $T_{i,0}=0.03$ eV. Test cases with different initial electron density and electron temperature are also performed. The modeling results show that the selection of initial plasma parameters scarcely changes the profiles at steady state. Three types of electron-neutral collisions, i.e., elastic scattering, excitation and ionization are included. The cross-section data used in the simulations are taken from Ref. [30, 31] and depicted in Appendix A. The ion-neutral collisions are neglected due to the very low bulk ion temperature and ion current density. The cell size $\Delta x=26.3$ μm is specified to resolve the Debye length (~54.3 μm, with a maximum plasma density 1.5×10^{17} m^{-3} at steady state) and the smallest collision free path (~0.11 m, corresponding to the electron-impact ionization in this study). The total number of grids is thus 1.43×10^{6} (189×7560 for $L_x\times L_y$). The time step $\Delta t=11.1$ ps is specified to resolve the electron plasma frequency ($\omega_{e,max}\Delta t<1$ with maximum $\omega_{e,max}=2.2\times10^{10}$ s^{-1}) as well as the smallest collision time (~4.3 ns corresponding to the electron-impact ionization). For a typical simulation time 15 μs, a total of 1.35×10^{6} time steps is needed. Initially, 100 macro-particles per cell are created for each species with a fixed particle weight $w=6.9\times10^{4}$ (Same value for beam electrons). During the simulation, the total number of macro-particles rises with the

increase of the plasma density until the steady state is attained. The steady state is defined as the condition where the plasma properties over several tens of ion plasma periods hardly change, namely a balance of ionization-produced ions and lost ions is achieved. All the simulations are carried out in Sugon high-performance cluster. The CPU time for each case is about 3~4 days, with the usage of 360 cores. The modeling parameters are summarized in Table I.

Table I. Simulation parameters for the cases discussed in Section III

Parameter	Symbol	Value	Unit
Configurations			
Cell size	Δx	26.3	μm
Time step	Δt	1.11×10^{-11}	s
Particle weight	w	6.9×10^4	
Longitudinal length	L_y	200	mm
Transversal length	L_x	5	mm
Injection electrode length	L_{inj}	3.3	mm
Initial conditions			
Plasma density	$n_{e,0}$	1×10^{16}	m^{-3}
Electron temperature	$T_{e,0}$	4.0	eV
Ion temperature	$T_{ion,0}$	0.03	eV
Operating conditions			
Gas Pressure	p	3~9	Pa
Gas temperature	T_{Ar}	300	K
Beam current density	J_b	300~1000	A/m^2
Beam energy	ε_b	2~8	keV

III. Results and Discussions

To meet the requirements of material processing, it is crucial to have an EBP system that delivers uniform ion flux and ion energy flux. In some particular applications, it is preferable to have a high ion flux with a relatively low ion energy flux to mitigate surface damage issues. Namely, the goal is to independently modulate the plasma density and electron temperature while keeping relatively good uniformity. Therefore, in this section, our primary focus lies in discussing these crucial plasma parameters. We begin with the typical 2D profiles for the base case in Section III(A). Subsequently, in Section III(B), case-dependent variations of the plasma parameters are explored.

A. Profiles of potential and EBP properties for base case

In this sub-section, we provide profiles of various plasma parameters for the base case, offering insights into the characteristics of the EBP system. The plasma parameters are examined including the potential φ, beam electron density n_b, bulk electron and ion number densities n_e and n_i, electron temperature $T_{e,x}$, electron and ion flux Γ_e and Γ_i, and ion energy flux to the wall $\Gamma_{\varepsilon,w}$. We note that in this paper, the term "beam electrons" refer to the electron populations injected from the injection electrode, and the term "bulk electrons" refer to the electron populations produced by ionization. The operating conditions for the base case are set as follows: beam current density $J_b=700$ A/m^2, beam energy $\varepsilon_b=4$ keV, and gap pressure $p=7$ Pa. The presented data correspond to the steady-state conditions of the plasma system. The profiles at the negative x range are generated by applying inversion symmetry.

1. Potential

Inherently, EBPs are complex systems characterized by the coupling of ionization and collective effects. The injected electron beam not only induces ionization within the plasma but also interacts with the produced plasmas, leading to the excitation of various wave phenomena. As illustrated in Fig. 2, a wave structure is clearly observed in the contours of potential. The wave structure initially emerges in the vicinity of the injection point due to the intense beam-plasma interaction. Subsequently, as the plasma evolves longitudinally, the amplitude of the wave structure grows, indicating a spatially growing mode [32, 33]. The maximum amplitude

reaches approximately 20 V, which is significant enough to trap the produced cold bulk electrons within the wave structure. At $y < 100$ mm, oscillations along the beam propagation direction ($+y$) are predominantly observed. However, at the region $y > 100$ mm, the wave packet exhibits a crescent shape (See Fig. 2), suggesting that the wave becomes oblique in nature [34, 35]. Namely, the wave vector is no longer aligned with the beam propagation direction. Thus, such wave structure introduces a perpendicular electric field component, deviating from the beam propagation direction. This perpendicular electric field interacts with the beam electrons, causing scattering and altering their transport characteristics. In this paper, we will only present the impact of these waves on the plasma parameters. and leave a detailed discussion of the wave behaviors to our companion paper.
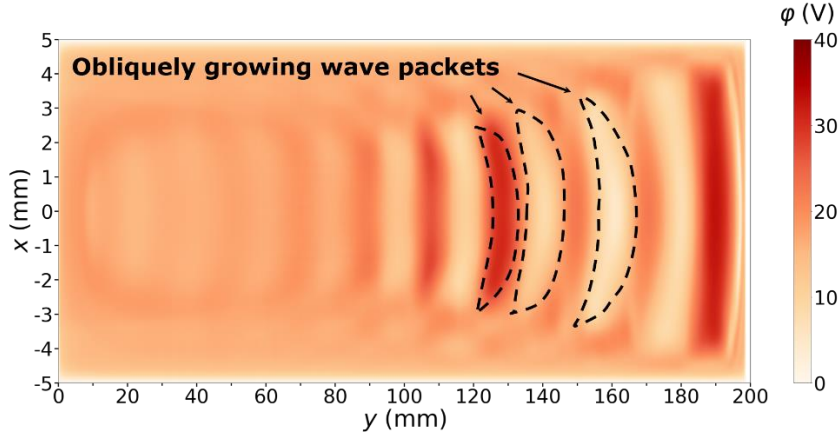

Fig. 2 Potential contours for base case with the operating conditions as J_b=700 A/m^2, ε_b=4 keV, p=7 Pa. Crescent-shape wave structures occur at $y > 100$ mm

2. Number densities of beam electrons, bulk electrons and ions

Fig. 3 shows the contours of the beam electron density n_b. In the region $y<100$ mm, the beam predominantly propagates along the y-direction, despite a slight bunching caused by the positive floating plasma potential. At $y\approx90$ mm, near the location where the wave transits to an oblique state, the beam electrons experience scattering and concentration, which leads to a significant non-uniformity in n_b. The value of n_b increases from 1.2×10^{16} m^{-3} to a local maximum value of 2.8×10^{16} m^{-3}, more than twice higher. As the beam propagates further, the amplitude of the density perturbation continues to increase. At the downstream region ($y>100$ mm), a fishbone-like density distribution emerges, with the majority of beam electrons concentrated at the skeleton. This formation of a fishbone density distribution signifies a strong

modification of the beam's behavior induced by the obliquely growing wave.
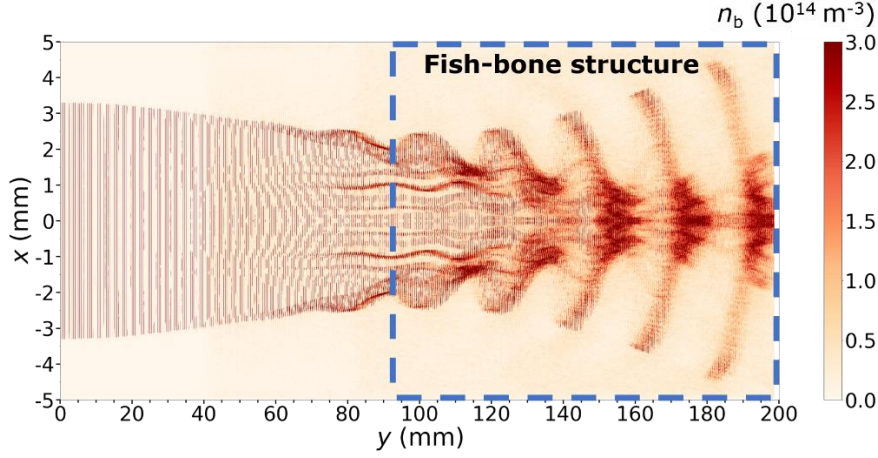

Fig. 3 Contours of beam density for base case with the operating conditions as J_b=700 A/m^2, ε_b=4 keV, p=7 Pa.

To further examine the impact of the excited wave on the plasma, we plotted the contours of the electron density n_e (a) and ion density n_i (b) in Fig. 4, and the distributions along transverse lines y=25 mm (c), y=100 mm (d) and y=175 mm (e). As shown in Figs. 4(a) and 4(b), the maximum plasma density reaches approximately 10^{17} m^{-3}. Visible boundaries can be observed, indicating three distinct regions:

(i) Bulk region: This region corresponds to the path of the electron beam and is characterized by relatively high plasma density (deeper red in Figs. 4(a) and 4(b)). In this region, plasmas are directly produced by the beam electron-impact ionization, resulting in a strong correlation between the distributions of n_e and n_i with that of n_b. A fishbone-like structure is evident, reflecting the influence of the obliquely growing waves on the beam transport. As shown in Figs. 4(c)~4(e), the values of n_e and n_i decrease transversely, creating a large density gradient that spreads out the ions. The non-uniformities in plasma density within this region are primarily attributed to the abnormal beam transport caused by the excitation of the obliquely growing waves;

(ii) Diffusion region: In this region, parabolic-like distributions of n_e and n_i are observed in Figs. 4(c) to 4(e), indicating the dominant role of diffusion. The ion flux increases as ions traverse through this region, as evidenced by Fig. 6 (see therein in this paper).

(iii) Sheath region. In this region, the quasi-neutrality condition is destroyed. The width of

the sheath remains almost constant along the y-axis, approximately 0.7 mm (equivalent to around 9 Debye lengths). The sheath voltage drop is ~12 V, in agreement with the predicted value for an argon floating sheath as $U_s=4.7T_{ex}/e \approx 11.8$ V ($T_{ex} \approx 2.5$ eV, see Fig. 5 therein) [36].
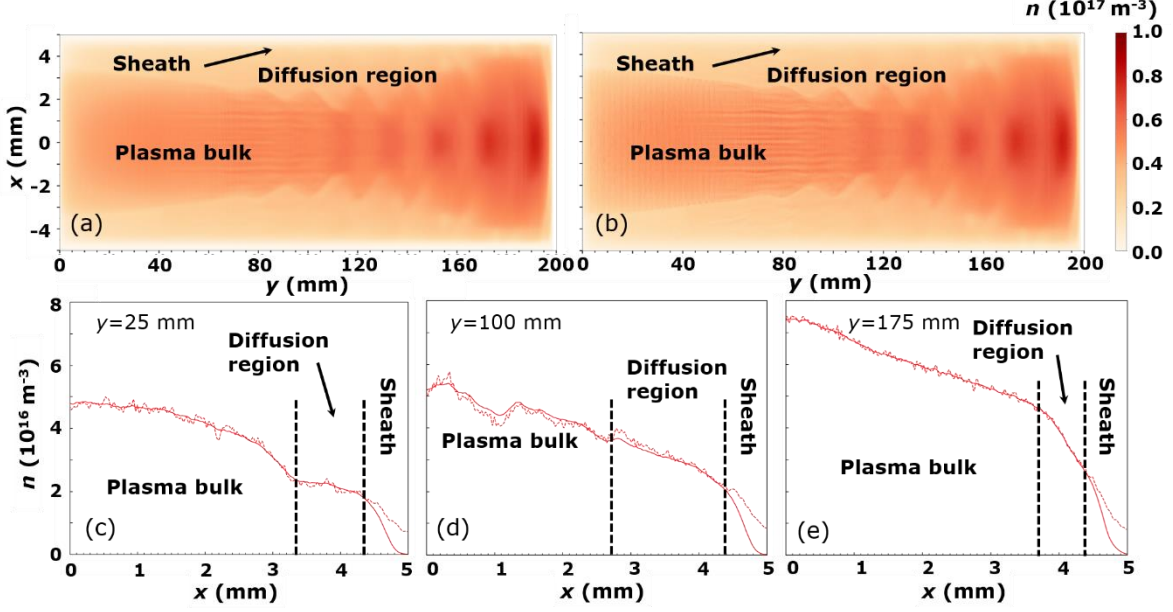

Fig. 4 Profiles of electron number density and ion number density. The contours of electron number density and ion number density are presented in (a) and (b), and the corresponding transverse distributions along $y=25$ mm, $y=50$ mm and $y=175$ mm are presented in (c)~(e) with solid line for electron and dashed line for ion. The operating conditions are $J_b=700$ A/m^2, $\varepsilon_b=4$ keV, $p=7$ Pa.
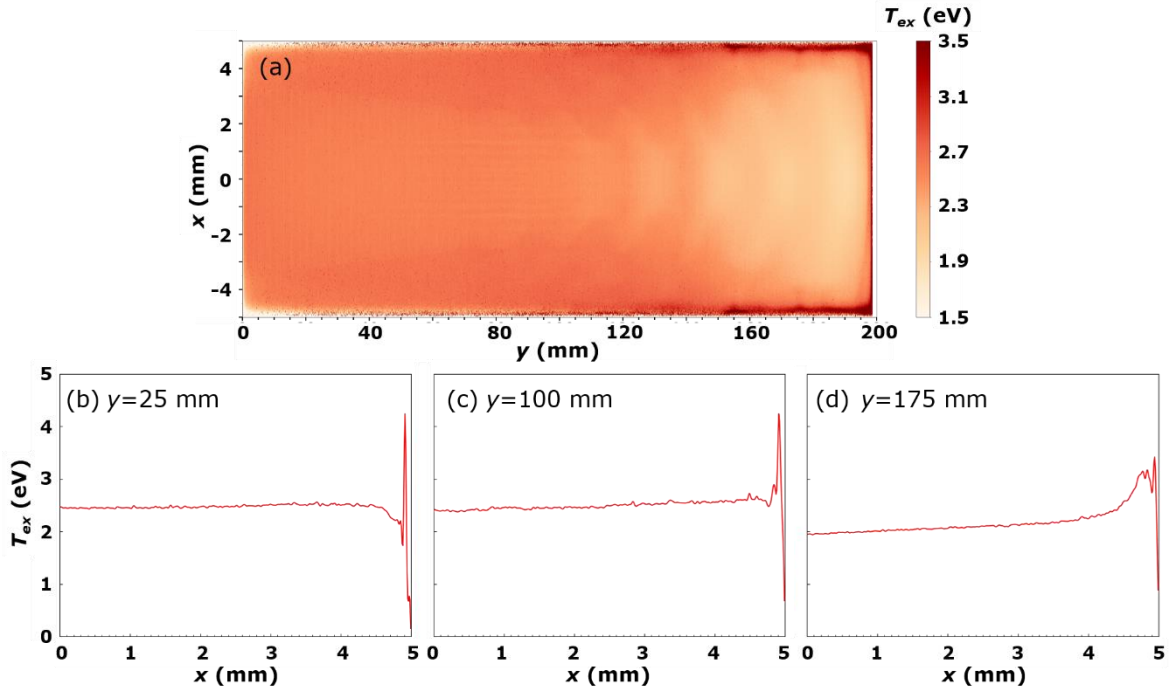
Fig. 5 Profiles of x component of bulk electron temperature T_{ex}. Contour of T_{ex} are presented in (a), and the corresponding transverse distributions along $y=25$ mm, $y=50$ mm and $y=175$ mm are presented in (b)~(d). The operating conditions are $J_b=700$ A/m^2, $\varepsilon_b=4$ keV, $p=7$ Pa.

3. Electron temperature

Fig. 5 shows: (a) contours of the x-component of bulk electron temperature T_{ex} (hereinafter referred to as electron temperature); (b)~(d) distributions of T_{ex} along the transverse lines at $y=25$ mm, 100 mm and 175 mm. Note that the y-component of the bulk electron temperature T_{ey} is not presented in this paper because it contributes negligibly to the transverse ion fluxes. Throughout the simulations, T_{ex} is computed at each grid node using the formula [37]

$$T_{ex} = m_e \left(\left\langle v_{e,x}^2 \right\rangle - \left\langle v_{e,x} \right\rangle^2 \right), \tag{1}$$

where m_e is the electron mass, $v_{e,x}$ is electron velocity in x direction, and $\langle \cdots \rangle$ denotes the average over the macroparticles of bulk electrons in each grid node. Beam electrons are not included in the calculation of T_{ex}. As illustrated in Fig. 5(a), T_{ex} decreases longitudinally from 2.5 eV to 1.9 eV within the bulk region, manifesting that the excitation of obliquely growing waves may result in a lowering of T_{ex}. The underlying mechanism behind this phenomenon is not yet fully understood. However, a qualitative explanation could be that the wave excitation enhances the population of tail electrons, leading to modifications in the rate coefficients for ionization, as discussed in Ref [38]. The typical electron velocity distribution functions and the contour of ionization rate are illustrated in Appendix B. It is worth noting that the simulated value of T_{ex} is slightly higher than the experimental measurement [14], which is attributed to the higher beam current density used in the simulation, being 2.5 times larger. In the transverse direction, T_{ex} exhibits a relatively uniform distribution, except for a peak occurring near the boundaries of the sheath and diffusion regions, as shown in Figs. 5(b) to 7(d). This phenomenon is attributed to the reflection of slow electrons by the sheath voltage drop and has also been observed in the literature [21].

4. Ion flux and ion energy flux

The paper presents the vector plot of the ion flux, Γ_i, over the entire simulation domain, as well as the distribution of the ion flux to the wall, $\Gamma_{i,w}$, are presented in Figs. 6(a) and 6(b),

respectively. Γ_i is computed at each grid node using the formula $\vec{\Gamma}_i = n_i \langle \vec{v}_i \rangle$. Fig. 6(a) illustrates that ions diffuse from the boundary of the bulk and diffusion regions, resulting in a noticeable increase in Γ_i. Apart from the longitudinal sheaths, the vectors of Γ_i are predominantly perpendicular to the wall surface, indicating negligible diffusion in the y-direction. Fig. 6(b) demonstrates a slight longitudinal increase in $\Gamma_{i,w}$ from 5.5×10^{19} m^{-2}·s^{-1} at y=10 mm to 7.0×10^{19} m^{-2}·s^{-1} at y=190 mm, despite some oscillations due to the non-uniformity of plasma density.
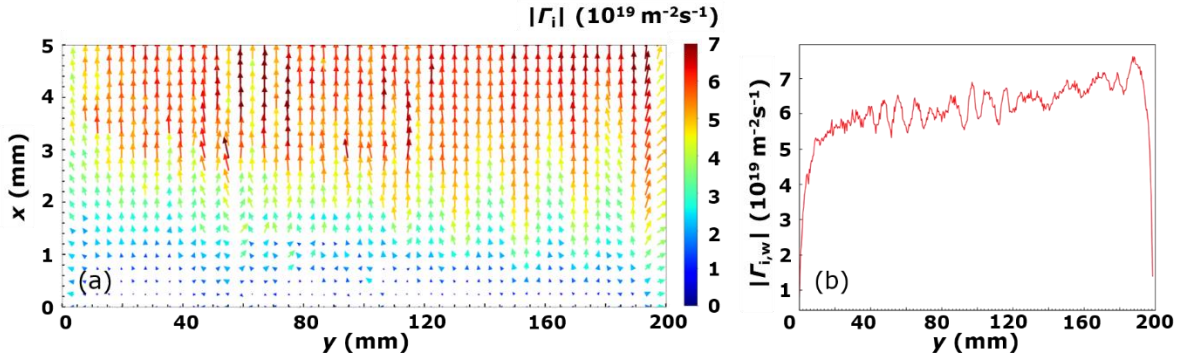

Fig. 6 Vector plot of ion flux Γ_i (a) and distributions of ion flux to the wall $\Gamma_{i,w}$ (b). The operating conditions are J_b=700 A/m^2, ε_b=4 keV, p=7 Pa.

The paper presents the vector plot of the ion energy flux, Γ_ε, over the entire simulation domain, as well as the distribution of the ion energy flux to the wall, $\Gamma_{\varepsilon,w}$, as shown in Figs. 7(a) and 7(b) respectively. The ion energy flux, Γ_ε, is computed at each grid node using the formula

$$\vec{\Gamma}_\varepsilon = m_i n_i \langle v_{i,x}^2 + v_{i,y}^2 + v_{i,z}^2 \rangle \langle \vec{v}_i \rangle, \tag{2}$$

where $v_{i;x,y,z}$ represents the ion velocity in x, y, and z directions. In the bulk, ion energy flux is low due to the low ion energy there. Ions gain energy primarily in the sheath region, thereby forming a large energy flux impacting the walls. As shown in Fig. 7(b), the oscillations of $\Gamma_{\varepsilon,w}$ are seen, which is because the waves can modify the plasma potential, and thus, affect the ion energy flux. The average $\Gamma_{\varepsilon,w}$ is approximately 8×10^{20} eV·m^{-2}·s^{-1}. Given $\Gamma_{i,w} \approx 6 \times 10^{19}$ m^{-2}·s^{-1}, the average energy that each ion carries is calculated as 13.3 eV, in agreement with the predicted energy of argon ions bombarding the wall as ε_i=5.2 $T_{ex} \approx$ 13.0 eV for an argon floating sheath [36].
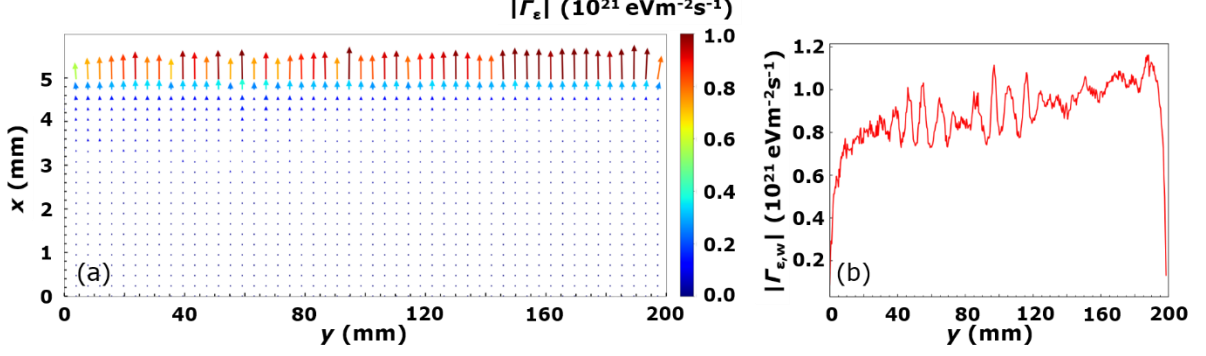
Fig. 7 Vector plot of ion energy flux Γ_ε (a) and distributions of ion energy flux to the wall $\Gamma_{\varepsilon,w}$ (b). The operating conditions are J_b=700 A/m^2, ε_b=4 keV, p=7 Pa.

It is worth highlighting that in Ref. [20], EBP discharges were also studied based by means of the PIC/MCC simulation. Notably, there are significant distinctions between the behavior of our EBP system and theirs:

(i) The modeling results of Ref. [20] demonstrated a diffusion-like profile for the steady-state plasma density across almost the whole discharge chamber, which differs from the observations in our simulations. This is because the transverse length of the chamber was much larger than the beam radius in their cases, resulting in plasma production primarily occurring in a very narrow region near the chamber center, followed by the spreading out of ions through diffusion. Consequently, a large diffusion region was formed.

(ii) Notably, the excitation of waves was not observed in their simulations. This observation may be attributed to the lower plasma density. Besides that, the diffusion process also has the potential to smooth out density perturbations.

B. EBP characterization for different cases and relevant discussions

In this subsection, a parametric study of the EBP properties is performed to study the impacts of different operating conditions (i.e. J_b, ε_b, and P) on the distributions of critical plasma parameters, i.e. n_e, T_e, $\Gamma_{i,w}$ and $\Gamma_{\varepsilon,w}$. The base case used for comparison is J_b=700 A/m^2, ε_b=4 keV, p=7 Pa, which is described in Sec III(A). All the data are collected from steady state and averaged over 100 snapshots within a 10 ns time interval to eliminate the numerical noises and fluctuations.

1. Plasma density profiles with varying J_b, ε_b, and p

Profiles of the electron number density along the y-axis $x=0$ mm under different conditions are shown in Fig. 8, organized according to the cases with varied (a) beam current density J_b, (b) beam energy ε_b, and (c) pressure p. Note that ion density profiles are not shown here as quasi-neutrality is maintained throughout most of the domain, except for the sheath region.

As shown in Fig. 8(a), the average value of n_e rises from approximately 2.5×10^{16} m^{-3} to around 8×10^{16} m^{-3} with J_b increasing from 300 A/m^2 to 1000 A/m^2. This trend is expected because n_b increases correspondingly with J_b. For the cases with $J_b=300$ and 500 A/m^2, n_e has a relatively flat distribution along the y-axis, despite some perturbations induced by waves. For the cases with $J_b=700$ and 1000 A/m^2, n_e exhibits a slope longitudinal distribution with higher value at larger y. This is because, on one hand, high-amplitude waves lead to local concentration of beam electrons and bulk plasma (see Figs. 3 and 4); on the other hand, beam electrons undergo energy loss through interactions with waves, resulting in enhanced ionization at $y>100$ mm as because the ionization cross-section becomes higher at low electron energies (see Appendix A).
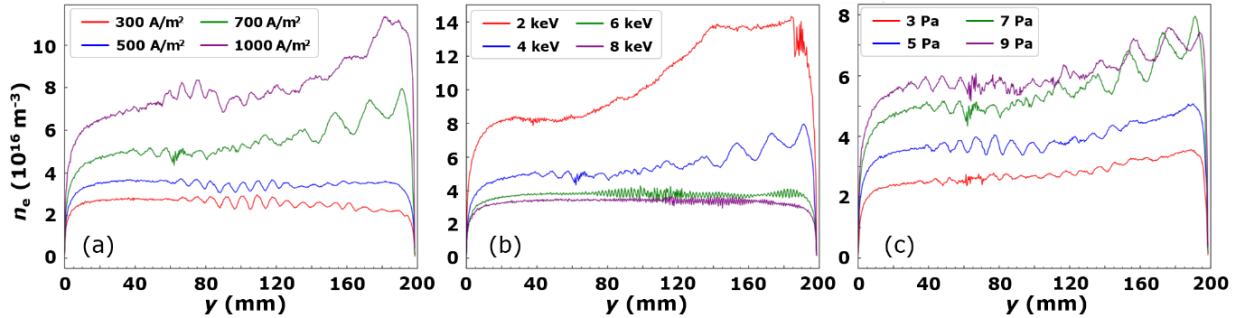

Fig. 8 Variations of electron number density profiles along the y-axis with (a) $J_b=300\sim1000$ A/m^2, (b) $\varepsilon_b=2\sim8$ keV, and (c) $p=3\sim9$ Pa. The operating conditions of the base case are $J_b=700$ A/m^2, $\varepsilon_b=4$ keV, $p=7$ Pa

Fig. 8(b) shows that n_e decreases with increasing ε_b. This trend is attributed to the decreasing of ionization rate with higher ε_b in the keV range. The ionization rate S_i can be evaluated as $\sim\sigma_{ei}n_a n_b v_b$, where σ_{ei} is the electron-impact ionization cross-section, n_b is the density of argon gas atom, and v_b denotes the beam electron velocity. For $\varepsilon_b>1.0$ keV, σ_{ei} varies as the inverse first power of ε_b, namely $\sigma_{ei}\sim\varepsilon_b^{-1}$ [39]. Therefore, $S_i \sim \sigma_{ei}n_b v_b \sim\sigma_{ei}\sim\varepsilon_b^{-1}$, indicating that the value of n_e falls with ε_b for $\varepsilon_b>1.0$ keV.

This mechanism also offers an explanation for the density hump observed in cases with ε_b=2 keV and 4 keV. As shown in Fig. 9, for the cases with ε_b=6 keV and 8 keV, the waves are weak with amplitudes of several Volts. However, for the cases with ε_b=2 keV and 4 keV, the high-amplitude waves with amplitudes of 20~30 V are clearly seen. A rigorous analysis for this phenomenon would be complicated due to the nonlinear nature of obliquely growing wave, which lies beyond the scope of this paper. For simplicity, a qualitative explanation is provided here. In a finite-size beam-plasma system, the wave number and spatial growth rate can be approximated based on linear theory [40].

$$
\begin{aligned}
\text{Re}(k) &\approx \frac{\omega_e}{v_b}\left[1.1+\frac{1+2.5\cos\left(L_n\right)}{1.1L_n}\right], \\
\text{Im}(k) &\approx \frac{\omega_e}{v_b}\frac{2\ln\left(L_n\right)-0.5}{L_n}
\end{aligned}
\tag{3}
$$

where ω_e denotes the electron frequency, and $L_n=L_y\omega_e/v_b$ denotes the normalized gap length. For the base case (J_b=700 A/m^2, ε_b=4 keV, and p=7 Pa), the theoretically predicted wavelength $\lambda_{\text{th}}=2\pi/\text{Re}(k)$ is 17 mm according to Eq. (3). This value aligns closely with the simulation result of $\lambda_{\text{sim}} \approx 20$ mm, thereby affirming the accuracy of Eq. (3). Apparently, with a fixed L_y, we have

$$
\begin{aligned}
\text{Re}(k) &\sim \omega_e v_b^{-1} \sim n_e^{1/2}\varepsilon_b^{-1/2} \sim S_i^{1/2}\varepsilon_b^{-1/2} \sim \varepsilon_b^{-1}, \\
\text{Im}(k) &\sim \ln\left(\omega_e v_b^{-1}\right) \sim \ln\left(\varepsilon_b^{-1}\right)
\end{aligned}
\tag{4}
$$

From Eq. (4), it is evident that both Re(k) and Im(k) decrease with increasing ε_b. This implies that waves with shorter wavelengths and higher spatial growth rates tend to occur at lower ε_b values, which is consistent with the simulation results shown in Fig. 9. When interacting with higher amplitude waves, beam electrons lose more energy. Consequently, in cases with ε_b=2 keV and 4 keV, beam energy decreases significantly near the end of the domain. Therefore, a higher ionization rate is achieved, leading to the formation of a prominent density hump there.
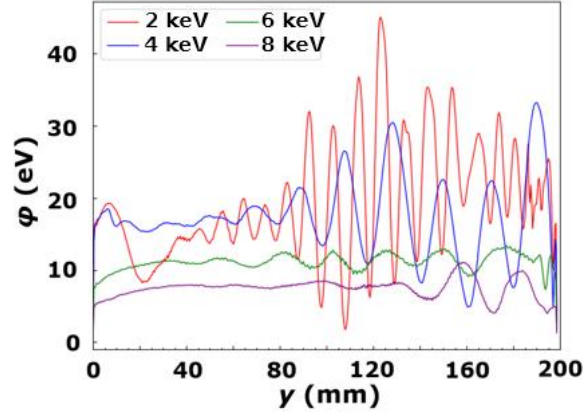
Fig. 9 Potential profiles along the y-axis for the cases with ε_b=2 kV, 4 kV, 6 kV and 8 kV. Other operating conditions are J_b=700 A/m^2, p=7 Pa

Fig. 8(c) illustrates that the average n_e increases from 2.5×10^{16} m^{-3} at p=3 Pa to 6×10^{16} m^{-3} at p=9 Pa. This trend is consistent with that of the ionization rate $S_i \sim n_a \sim p$. Additionally, similar density humps at the end of the simulation domain are observed across the different pressure values. The density gradient becomes more pronounced with increasing pressure because beam electrons experience more collisions with atoms at higher pressures, leading to a greater energy loss.

2. Electron temperature profiles with varying J_b, ε_b, and p

Fig. 10 summarizes the profiles of T_{ex} along the y-axis for the cases with varied J_b, ε_b, and p. As depicted in Figs. 10(a) and 10(b), T_{ex} is highly dependent on the beam parameters (i.e. J_b and ε_b). For the cases with J_b=300 and 500 A/m^2 , as well as the cases with ε_b=6 keV and 8 keV, T_{ex} exhibits relatively flat distributions along the y-axis. However, for the cases with J_b=700 and 1000 A/m^2, as well as the cases with ε_b=2 keV, 4 keV, T_{ex} falls longitudinally until reaching the boundary of the end electrode sheath. This is, as discussed in the second subsection of Section III(A), probably attributed to the modification of the electron energy distribution by obliquely growing waves. The value of T_{ex} is 1.1 eV for cases with J_b=300 A/m^2, ε_b=4 keV, and p=7 Pa, agreeing with the measured T_{ex} of approximately 1 eV under the experimental condition in Ref. [14] with $J_b \approx 260$ A/m^2, ε_b=4 keV and p=7 Pa. The maximum difference in T_{ex}, as p varied from 3 Pa to 7 Pa, is only 0.3 eV, indicating that T_{ex} is relatively insensitive to the changes of gas pressure.
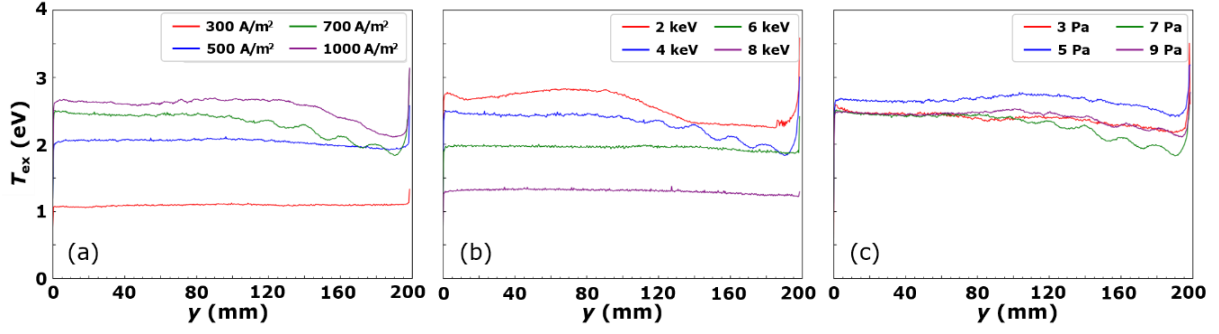
Fig. 10 Variations of electron temperature profiles along the y-axis with (a) J_b=300~1000 A/m^2, (b)ε_b=2~8 keV, and (c) p=3~9 Pa. The operating conditions of the base case are J_b=700 A/m^2, ε_b=4 keV, p=7 Pa

3. Profiles of ion flux and ion energy flux with varying J_b, ε_b, and p

Fig. 11 and Fig. 12 present the profiles of the wall-collected ion flux $\Gamma_{i,w}$ and ion energy flux $\Gamma_{\varepsilon,w}$ with varying J_b, ε_b, and p. It is observed that, in general, both $\Gamma_{i,w}$ and $\Gamma_{\varepsilon,w}$ exhibit an increasing trend with J_b but a decreasing trend with ε_b within the parameter ranges of interest. For an argon floating sheath,

$$\Gamma_{i,w} \sim n_e v_{Bohm} \sim n_e \sqrt{\frac{T_{ex}}{m_i}}, \quad \Gamma_{\varepsilon,w} \sim \Gamma_{i,w} \cdot 5.2 T_{ex} \sim 5.2 n_e \frac{T_{ex}^{3/2}}{\sqrt{m_i}} , \tag{5}$$

where v_{Bohm}=$(T_{ex}/m_i)^{1/2}$ denotes the Bohm speed with m_i being the ion mass. $\Gamma_{i,w}$ is on the order of 10^{19} m^{-2}s^{-1} and $\Gamma_{\varepsilon,w}$ on the order of 10^{20} eV·m^{-2}s^{-1}, consistent with the values predicted by Eq. (5), given n_e~10^{16} m^{-3} and T_{ex} in the range of few electron volts. As shown in Figs. 11(a)~(b) and Fig. 12(a)~(b), for the cases with J_b=300 and 500 A/m^2, as well as the cases with ε_b=6 keV, 8 keV, $\Gamma_{i,w}$ and $\Gamma_{\varepsilon,w}$ exhibit relatively uniform distributions, which is consistent with the relatively flat profiles of n_e and T_{ex} (see Figs. 8 and 10). For the cases with J_b=700 and 1000 A/m^2, as well as the cases with as ε_b=2 keV, 4 keV, although n_e and T_{ex} are not uniform, they exhibit the opposite longitudinal variations (n_e increases while T_{ex} decreases). Consequently, the non-uniformities in n_e and T_{ex} compensate for each other according to Eq. (5). As a result, $\Gamma_{i,w}$ and $\Gamma_{\varepsilon,w}$ are more uniform than n_e and T_{ex}. It is worth noting that the variations of $\Gamma_{i,w}$ and $\Gamma_{\varepsilon,w}$ with p are primarily dependent on that of n_e since T_{ex} is not sensitive to p,. As shown in Figs. 11(c) and 12(c), $\Gamma_{i,w}$ and $\Gamma_{\varepsilon,w}$ increase from approximately 2.5×10^{19} m^{-2}s^{-1} and 5×10^{20} eV·m^{-2}s^{-1} at p=3 Pa to around 7×10^{19} m^{-2}s^{-1} to 9×10^{20} eV·m^{-2}s^{-1} at p=9 Pa, resembling the trend of n_e despite some discrepancy due to the small variations in T_{ex}.
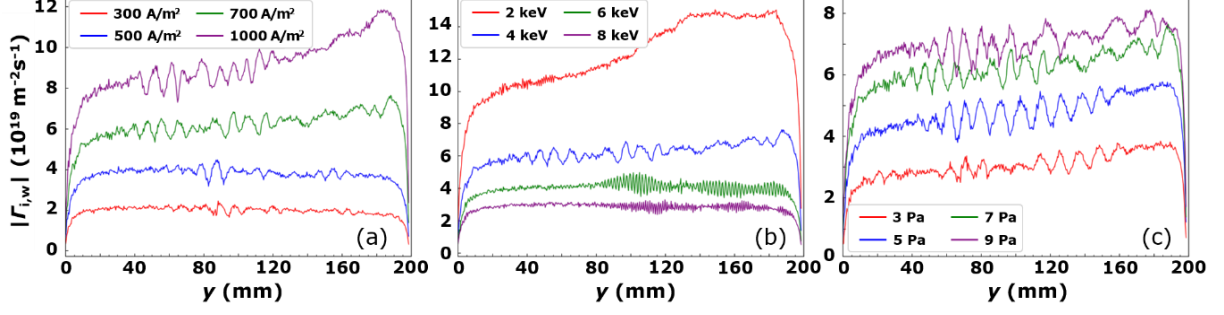
Fig. 11 Variations of the ion flux to the wall with (a) J_b=300~1000 A/m^2, (b)ε_b=2~8 keV, and (c) p=3~9 Pa.

The operating conditions of the base case are J_b=700 A/m^2, ε_b=4 keV, p=7 Pa

Fig. 12 Variations of the ion energy flux to the wall with (a) J_b=300~1000 A/m^2, (b)ε_b=2~8 keV, and (c) p=3~9 Pa. The operating conditions of the base case are J_b=700 A/m^2, ε_b=4 keV, p=7 Pa

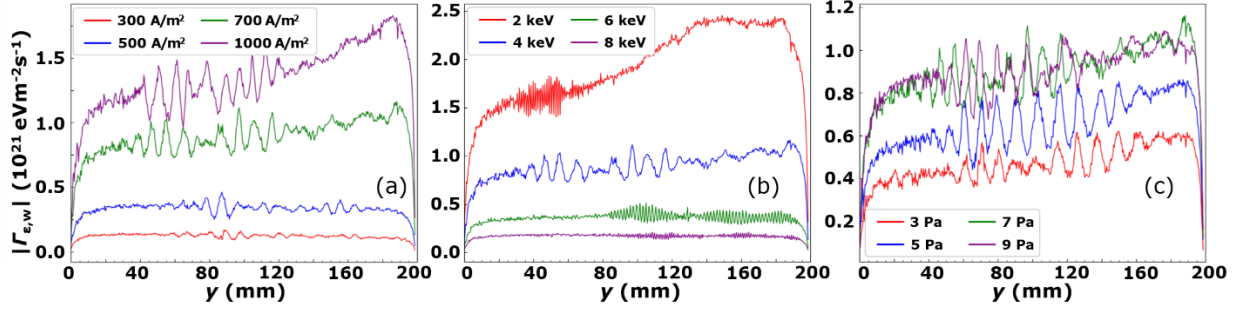To sum up, the parametric study reveals that increasing the beam current density (J_b) results in higher plasma density, but also leads to higher electron temperatures and larger non-uniformities. Conversely, increasing the beam energy decreases the electron temperature and smooth out the profiles, yet it also leads to the decreasing of plasm density. These contrasting trends differ from the observations in micro-discharge EBPs [21], which pose a challenge in tuning the ion flux and ion energy flux sorely by adjusting the beam current density and beam energy for transversely confined EBPs, as they have opposing effects that tend to compensate each other. Fortunately, it is observed that adjusting the pressure has a significant impact on plasma density while having minimal effect on electron temperature. This provides an opportunity to independently modulate plasma density and electron temperature through integrated control of beam current density, beam energy and pressure.

For instance, achieving a lower energy flux while keeping the ion flux constant can be accomplished by, at first, reducing the beam current density (or increasing the beam energy) to lower the electron temperature. However, this practice also leads to a decrease in plasma

density. To counteract the decrease in plasma density and maintain a constant ion flux, one can then precisely increase the pressure to lift up the plasma density. By employing these strategies, independent control over the ion flux and energy flux can be possibly achieved. Furthermore, it is noticed that reducing the beam current density (or increasing the beam energy) leads to a visible enhancement in the uniformity of ion flux to the wall and energy flux, while increasing the background pressure causes less pronounced disturbance to uniformity. Therefore, it is reasonable to expect that employing these strategies should not worsen the plasma uniformity but may even improve it.

IV. Summary and conclusions

In this paper, we employ a two-dimensional PIC/MCC model to investigate the characteristics of argon EBPs transversely confined within a narrow gap. The model simulates the generation of plasmas through mono-energetic beams emitted from the injection electrode. Such process resembles the inner surface treatment of tubular apparatuses in practical applications. Our PIC/MCC model incorporates the electron and Ar^+ kinetics as well as the electron-neutral collisions including the elastic scattering, excitation and impact ionization. The primary conclusions are summarized as follows:

(1) Three regions are distinguished. Plasma production primarily occurs in the bulk region along the path of the electron beam. The density gradient at the bulk boundaries leads to ion diffusion into the diffusion region, where the ion flux gradually increases. Near the wall, a floating sheath is formed, and ions primarily gain energy in this sheath, resulting in a significant ion energy flux towards the surface.

(2) Obliquely growing waves with crescent-shaped potential structures are found to be excited and significantly modify the beam transport, thereby leading to a fishbone-like distribution of beam density. In the bulk region, electron and ion number densities are tightly correlated with the beam density and are strongly influenced by the waves. Electron temperature is also found to be reduced by the presence of obliquely growing waves in this region. However, the properties of the plasma in the diffusion and sheath regions remain unaffected by the waves.

(3) The plasma density exhibits a slope longitudinal distribution with a hump near the end,

resulting from the energy loss of beam electrons due to their interactions with the waves. On the other hand, the electron temperature shows an inverse distribution with the value decreasing longitudinally. These opposite trends of plasma density and electron temperature compensate for each other to some extent, smoothing the longitudinal flux distributions.

(4) Variations of the plasma parameters with respect to the beam current density J_b, beam energy ε_b and gas pressure p are examined. It is found that increasing J_b or decreasing ε_b leads to higher plasma density and electron temperature, as well as larger non-uniformities; while increasing p results in a higher plasma density but scarcely changes the electron temperature. It means that, for the EBPs transversely confined in a narrow gap, increasing J_b and decreasing ε_b play the inverse roles in modulating n_e and T_{ex}, which make it challenging to independently tune the ion flux and ion energy flux sorely by adjusting J_b and ε_b. Therefore, we suggest an approach involving the integrated adjustment of beam current density, beam energy, and pressure.

It should be noted that this study does not account for the effects of secondary electron emission and chemical reactions and collisions between ions and neutrals. These factors may become significant when applied to EBPs in the presence of an extraction electric field or in the presence of a molecular gas (e.g., nitrogen). These effects will be investigated in our future work. Moreover, the present work does not incorporate cylindrical effect. That requires the implementation of a cylindrical model and will be investigated in our future work.

Acknowledgement

Conflict of Interest

There are no conflicts of interest to declare

Data availability statement

The data that support the findings of this study are available from the corresponding author upon reasonable request.

Appendix A: Cross-section data

This appendix summarizes the cross-section data used in the simulations. As depicted in Fig. 13, the ionization cross-section (blue curve) decreases with projectile energy ε in the range ε>1 keV.
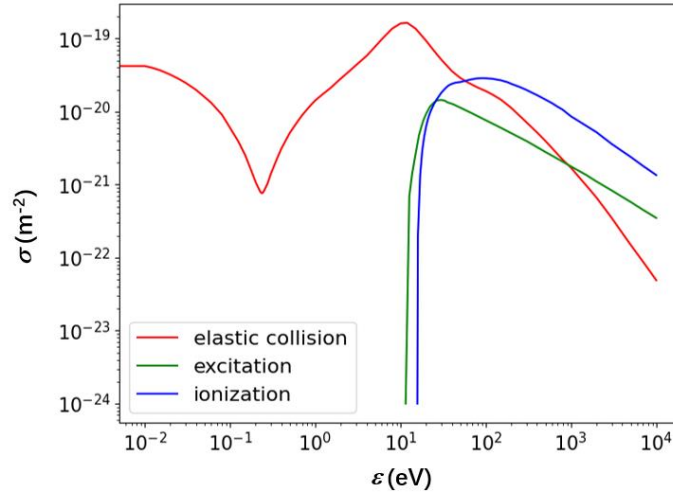
Fig. 13 Cross section as a function of projectile energy used in the simulations

Appendix B: Electron velocity distribution functions and contours of ionization rate

This appendix summarizes the typical electron velocity distribution functions (EV$_x$DF) and the contours of ionization rate for base case with the operating conditions as J_b=700 A/m^2, ε_b=4 keV, p=7 Pa, which are plotted in Figs. 14 and 15, respectively.

Fig. 14 shows the main body and tail of EV$_x$DFs at steady state for base case (J_b=700 A/m^2, ε_b=4 keV, p=7 Pa). The red and blue curves represent the EV$_x$DFs at the upstream region (0<x<1.67 mm, 0<y<50 mm) and the downstream region (0<x<1.67 mm, 150<y<200 mm), respectively. Note that the EV$_x$DFs are normalized using the total number of electrons contained within the respective regions. Note that the EV$_x$DFs are calculated by accounting for

all the bulk electrons contained within the respective regions and normalized using the total number of bulk electrons.

As shown in Fig. 14(a), the main body of EV_xDF at the upstream region exhibits a slightly broader distribution compared to its downstream counterpart, agreeing with the observation where the electron temperature drops from the upstream to downstream region. Conversely, the population of high-energy electrons, referred to as the tail of the EV_xDF, is more pronounced in the downstream region than in the upstream region (see Fig. 14(b)), suggesting an enhancement in the tail of the EV_xDF in the downstream region. These behaviors of EV_xDF are consistent with the predictions presented in Ref. [38], which demonstrate that the enhancement of tail electrons modifies the ionization rate coefficient, resulting in the decrease of electron temperature.

In Fig. 15, the ionization rate demonstrates a strong correlation with wave behaviors, indicating a significant modification of the ionization rate by the waves.
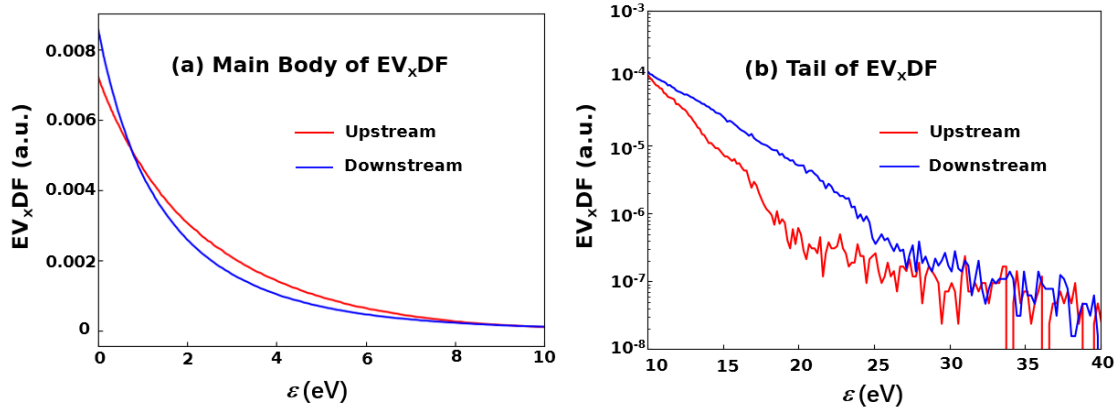

Fig. 14 Main body (a) and tail (b) electron velocity distribution function at steady case for base case (J_b=700 A/m^2, ε_b=4 keV, p=7 Pa). The red and blue curves show the electron velocity distribution functions at the upstream region (0<x<1.67 mm, 0<y<50 mm) and the downstream region (0<x<1.67 mm, 150<y<200 mm), respectively. The EV_xDFs are calculated by accounting for all the bulk electrons contained within the respective regions and normalized using the total number of bulk electrons.
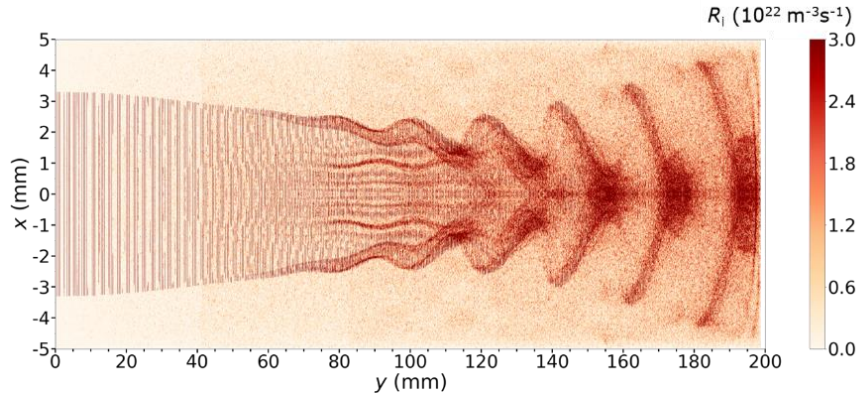
Fig. 15 Contours of ionization rate for base case with the operating conditions as J_b=700 A/m^2, ε_b=4 keV, p=7 Pa.

References

1. Burdovitsin V A, Klimov A S and Oks E M 2009 On the possibility of electron-beam processing of dielectrics using a forevacuum plasma electron source *Technical Physics Letters* **35** 511-3.

2. Lock E H, Petrovykh D Y, Mack P, Carney T, White R G, Walton S G and Fernsler R F 2010 Surface composition, chemistry, and structure of polystyrene modified by electron-beam-generated plasma *Langmuir* **26** 8857-68.

3. Walton S, Boris D R, Hernández S C, Lock E H, Petrova T B, Petrova G M and Fernsler R F 2015 Electron beam generated plasmas for ultra low T_e processing *ECS Journal of Solid State Science and Technology* **4** N5033.

4. Oks E M, Tyunkov A V, Yushkov Yu G and Zolotukhin D B 2017 Ceramic coating deposition by electron beam evaporation *Surface and Coatings Technology* **325** 1-6.

5. Yushkov Y G, Oks E M, Tyunkov A V and Zolotukhin D B 2022 Electron-beam synthesis of dielectric coatings using forevacuum plasma electron sources *Coatings* **12** 82.

6. Reeves G D, Delzanno G L, Fernandes P A, Yakymenko K, Carlsten B E, Lewellen J W, Hollowway M A, Nguyen D C, Praff R F, Farrell W M, et al. 2020 The beam plasma interactions experiment: An active experiment using pulsed electron beams *Frontiers in Astronomy and Space Sciences* **7** 23.

7. Xue B -X, Hao J -H, Zhao Q and Dong Z -W 2020 Influence of geomagnetic field on the long-range propagation of relativistic electron beam in the atmosphere *IEEE Transactions on Plasma Science* **48** 3871-3876.

8. Ueda M, Silva C, Souza G B de, Mariano S F M, Pichon L 2018 Overcoming sheaths overlapping in a small diameter metallic tube with one end closed and using a high density plasma from a high power pulsed hollow cathode discharge *AIP advances* **8** 085103.

9. Chen F F 2012 *Introduction to plasma physics*. Springer Science & Business Media.

10. Kolev St, Hagelaar G J M, Fubiani G and Boeuf J -P 2012 Physics of a magnetic barrier in low-temperature bounded plasmas: insight from particle-in-cell simulations *Plasma Sources Science and Technology* **21** 025002.

11. Lichtenberg A and Jayson J 1965 Propagation and Instabilities of Waves in Bounded Finite Temperature Plasmas *Journal of Applied Physics* **36** 449-455.

12. Akhiezer, A I, Akhiezer, I A, Polovin R V, Sitenko A G and Stepanov K N 1975 *Plasma electrodynamics. Volume 1-Linear theory. Volume 2-Non-linear theory and fluctuations.* Oxford Pergamon Press International Series on Natural Philosophy **1**.

13. Burdovitsin V A, Bakeev I Y, Karpov K I and Oks E M 2022 Plasma generation in a long, narrow, metal tube by electron beam injection *Plasma Sources Science and Technology* **31** 055008.

14. Burdovitsin V A, Karpov K I, Bakeev I Yu and Oks E M 2022 Discharge in a long metal tube with an electron beam generated by a forevacuum plasma-cathode electron source *Physics of Plasmas* **29** 093503.

15. Zolotukhin D B, Burdovitsin V A and Oks E M 2015 Generation of uniform electron beam plasma in a dielectric flask at fore-vacuum pressures *Plasma Sources Science and Technology* **25** 015001.

16. Lock E H, Fernsler R F, Slinker S P, Singer I L and Walton S G 2014 Global model for plasmas generated by electron beams in low-pressure nitrogen *Journal of Physics D: Applied Physics* **47** 425206.

17. Chelvam P K P and Raja L L 2015 Computational modeling of the effect of external electron injection into a direct-current microdischarge *Journal of Applied Physics* **118** 243301.

18. Petrov G M, Boris D R, Petrova T B and Walton S G 2016 One-dimensional Ar-SF6 hydromodel at low-pressure in e-beam generated plasmas *Journal of Vacuum Science & Technology A: Vacuum, Surfaces, and Films* **34** 021302.

19. Rauf S, Balakrishna A, Agarwal A, Dorf L, Collins K, Boris D R and Walton S G 2017 Three-dimensional model of electron beam generated plasma *Plasma Sources Science and Technology* **26** 065006.

20. Rauf S, Sydorenko D, Jubin S, Villafana W, Ethier S, Khrabrov A and Kaganovich I 2023 Particle-in-cell modeling of electron beam generated plasma *Plasma Sources Science and Technology* **32** 055009.

21. Wang Y, Zhou Y -Y, Wu H, Zhang Y, Jiang W and Lapenta G 2022 Computational study

of microdischarges driven by electron beam injection with particle-in-cell/Monte Carlo collision simulations *Journal of Applied Physics* **131** 163301.

22. Huang J -L, Wang C, Chang L -J, Zhang Y, Wang Z -B and Jiang W 2019 Computational characterization of electron-beam-sustained plasma *Physics of Plasmas* **26** 063502.

23. Birdsall C K and Langdon A B 2004 *Plasma physics via computer simulation*. CRC press.

24. Boris J P 1970 Relativistic plasma simulation-optimization of a hybrid code *Proceedings of Fourth Conference on Numerical Simulations of Plasmas* Section **I** 3

25. May M, Khrabrov A, Sydorenko D and Kaganovich I 2021 Investigation of sheath electron temperature in RF capacitively-coupled plasmas using PIC simulations. in: *APS Division of Plasma Physics Meeting* 2021.

26. Sydorenko D 2006 *Particle-in-cell simulations of electron dynamics in low pressure discharges with magnetic fields*. University of Saskatchewan: Saskatoon.

27. Sun H -M, Banerjee S, Sharma S, Powis A T, Khrabrov A V, Sydorenko D, Chen J and Kaganovich I 2023 *Direct Implicit and Explicit Energy-Conserving Particle-in-Cell Methods for Modeling of Capacitively-Coupled Plasma Devices*. arXiv:2306.01581.

28. Villafana W, Petronio F, Denig A C, Jimenez M J, Eremin D, Garrigues L, Taccogna F, Alvarez-Laguna A, Boeuf J P and Bourdon A 2021 2D radial-azimuthal particle-in-cell benchmark for E× B discharges *Plasma Sources Science and Technology* **30** 075002.

29. Charoy T, Boeuf J P, Bourdon A, Carlsson J A, Chabert P, Cuenot B, Eremin D, Garrigues L, Hara K and Kaganovich I 2019 2D axial-azimuthal particle-in-cell benchmark for low-temperature partially magnetized plasmas *Plasma Sources Science and Technology* **28** 105010.

30. Hayashi M 2003 *Bibliography of electron and photon cross sections with atoms and molecules published in the 20th century. Argon*.

31. Phelps A V 1991 Cross sections and swarm coefficients for nitrogen ions and neutrals in N_2 and argon ions and neutrals in Ar for energies from 0.1 eV to 10 keV *Journal of Physical and Chemical Reference Data* **20** 557-573.

32. Sun H -M, Chen J, Kaganovich I D, Khrabrov A V and Sydorenko D 2022 Electron Modulational Instability in the Strong Turbulent Regime for an Electron Beam Propagating in a Background Plasma *Physical Review Letters* **129** 125001.

33. Sun H -M, Chen J, Kaganovich I D, Khrabrov A V and Sydorenko D 2022 Physical regimes of electrostatic wave-wave nonlinear interactions generated by an electron beam propagating in a background plasma *Physical Review E* **106** 035203.

34. Lu Q -M, Lembege B, Tao J B, Wang S 2008 Perpendicular electric field in two‐dimensional electron phase‐holes: A parameter study *Journal of Geophysical Research: Space Physics* **113** A11219.

35. Piel A, Klindworth M, Arp O, Melzer A, Wolter M 2006 Obliquely propagating dust-density plasma waves in the presence of an ion beam *Physical review letters* **97** 205009.

36. Lieberman M A and Lichtenberg A J 2005 *Principles of plasma discharges and materials processing.* John Wiley & Sons, Inc., Second Edition.

37. Schunk R W 1977 Mathematical structure of transport equations for multispecies flows *Reviews of Geophysics* **15** 429-445.

38. Haas F A, Goodyear A and Braithwaite N St J 1998 Tailoring of electron energy distributions in low temperature plasmas *Plasma Sources Science and Technology* **7** 471.

39. Jin B -M, Chen J, Khrabrov A V, Wang Z -B and Xu L 2022 Particle-in-cell simulations of the direct-current argon breakdown process in the 10-300 kV range *Plasma Sources Science and Technology* **31** 115015.

40. Kaganovich I D and Sydorenko D 2016 Band structure of the growth rate of the two-stream instability of an electron beam propagating in a bounded plasma *Physics of Plasmas* **23** 112116.